

Barycentric-alignment and invertibility for domain generalization

Boyang Lyu¹, Thuan Nguyen^{1,3}, Prakash Ishwar², Matthias Scheutz³, Shuchin Aeron^{1*}

June 19, 2022

Abstract

We revisit the problem of Domain Generalization (DG) where the hypotheses are composed of a common representation mapping followed by a labeling function. Popular DG methods optimize a well-known upper bound to the risk in the unseen domain. However, the bound contains a term that is not optimized due to its dual dependence on the representation mapping and the unknown optimal labeling function for the unseen domain. We derive a new upper bound free of the term having such dual dependence by imposing mild assumptions on the loss function and an invertibility requirement on the representation map when restricted to the low-dimensional data manifold. The derivation leverages old and recent *transport inequalities* that link optimal transport metrics with information-theoretic measures. Our bound motivates a new algorithm for DG comprising Wasserstein-2 barycenter cost for feature alignment and mutual information or autoencoders for enforcing approximate invertibility. Experiments on several datasets demonstrate superior performance compared to well-known DG algorithms.

1 Introduction

In many practical applications of modern machine learning, the training (seen) data and the test (unseen) data may belong to different *domains*, leading to loss of predictive power of the learned models. For example, a model trained on data from one hospital may not work well when the test data is from another hospital [Gulrajani and Lopez-Paz, 2020], a drowsiness driving estimator trained on one group of subjects does not generalize well for other subjects [Cui et al., 2019], a cognitive workload estimator from fNIRS (Fourier Near-Infrared Sensor) measurements may not generalize well across sessions and subjects [Lyu et al., 2021].

These types of problems are broadly classified into two categories, viz., Domain Adaptation (DA) [Ben-David et al., 2007] and Domain Generalization (DG) [Blanchard et al., 2011]. Both DA and DG aim to find a model that can generalize well when the seen domain training data does not share the same distribution with the testing data from the unseen domain. The key difference between DA and DG is that DA allows access to the (unlabeled) unseen domain data during the training process while DG does not, leading to a more challenging problem. For an extensive survey and related set of

^{*1} - Tufts University, Dept. of ECE, ² - Boston University, Dept. of ECE, ³ - Tufts University, Dept of CS.
Corresponding authors: Boyang Lyu, email: Boyang.Lyu@tufts.edu.

literature we refer the reader to excellent recent surveys [Wang et al., 2021, Zhou et al., 2021b] for DG, and [Redko et al., 2020] for DA.

To address the problem of DG, motivated by the seminal works of Ben-David et al. [2007, 2010], one usually parameterizes the hypothesis as composed of a representation function followed by a labeling function [Albuquerque et al., 2019, Dou et al., 2019, Li et al., 2018b, Zhou et al., 2021a]. The essential insight from the upper bound derived in [Ben-David et al., 2007, 2010] is that the risk on the unseen domain is upper bounded by three terms: (1) the prediction risk on the mixture of seen domains, (2) discrepancy or divergence between the data distributions in the representation space, and (3) a *combined risk* across all domains that is implicitly dependent on both the representation map and the unknown optimal labeling function from the unseen domain. Due to this dual dependency, most of the existing work ignores optimizing the third term (*combined risk*) and treats it as a constant for a given representation map. Having the *combined risk* ignored, a large body of the DG (as well as DA) methods [Ajakan et al., 2014, Ganin et al., 2016, Zhao et al., 2018, 2019] are essentially based on a variation of the following theme - learn a domain invariant representation mapping *or* align the domains in the representation space, while learning a common labeling function controlling the prediction loss across the seen domains. However, it is worth noticing that the *combined risk* is actually a function of the representation map, and hence needs to be part of the optimization. A detailed analysis of the shortcomings of the previous studies is provided in our Supplementary A.1.

1.1 Main Contributions

To address the shortcoming discussed above, we first make a mild assumption that the class of representation mappings are (nearly) invertible when restricted to distributions that lie on low-dimensional manifolds, well-known as the manifold-hypothesis [Lei et al., 2020]. Under this assumption, we derive a new upper bound for the risk in the representation space comprising three terms: (1) the prediction risk across seen domains in the input space; (2) the discrepancy/divergence between the induced distributions of seen and unseen domains in representation space that can be expressed in terms of the Wasserstein-2 Barycenter [Santambrogio, 2015] of the seen domains. For this we leverage old and new *transport inequalities* which also help avoid an additional Lipschitz assumption on the loss function that is typically assumed in related works; and (3) a *combined risk* term that is a constant with respect to the representation map and the labeling function to be learned. A detailed comparison between previous bounds and our work can be found in Supplementary A.1.

Our (manifold-restricted) invertibility assumption provides a natural justification for the use of an auto-encoder-like mechanism, which to date had been heuristically motivated in [Li et al., 2018b, Ghifary et al., 2015]. Moreover, to avoid introducing additional parameters to train for, namely the decoder, we propose the use of mutual information between the data and the representation as a surrogate for enforcing the approximate invertibility of the representation map. It may appear that having both invertibility and alignment is counter-intuitive but note that the alignment requirement does not preclude invertibility and vice-versa. Indeed, there are infinitely many (manifold-restricted) invertible maps for any given data manifold, and there could exist one which can align several domains

simultaneously.

Finally, based on these theoretical insights, we propose two novel algorithms, namely Wasserstein Barycenter Auto-Encoder (WBAE) and Wasserstein Barycenter Mutual Information (WBMI). The proposed algorithms leverage recent advances in the fast and efficient computation of Wasserstein barycenters as well as advances in computing reliable gradients of mutual information loss for implicit models from samples. We also note that the proposed algorithms completely bypass the use of any adversarial mechanism for domain alignment in the representation space.

1.2 Related Work

In [Albuquerque et al., 2019], the authors propose a model consisting of three parts: a feature extractor, a classifier, and domain discriminators. The feature extractor learns the task-sensitive but domain-invariant feature via minimizing the cross entropy loss w.r.t the task label and maximizing the sum of domain discriminator loss. The domain discriminator loss is treated as an estimation of \mathcal{H} divergence between all source domains [Ben-David et al., 2010]. Zhou et al. [2020] use the pairwise Wasserstein-1 distance [Santambrogio, 2015, Peyré and Cuturi, 2019], to estimate the divergence between different source domains. Utilizing the dual form of the Wasserstein-1 distance, the feature extractor minimizes a combination of cross entropy loss, Wasserstein distance loss, and a contrastive loss to achieve DG. Dou et al. [2019] adopt a gradient-based episodic training scheme for DG, with extracted features keeping the structure of the class relationship and the task-related clusters via minimization of alignment loss of soft-confusion matrix and a contrastive loss [van den Oord et al., 2018]. For an in-depth and comprehensive survey of such methods, we refer the reader to the excellent Appendix A.1 of [Gulrajani and Lopez-Paz, 2020].

2 THEORETICAL ANALYSIS AND PROPOSED METHODS

A *domain* v is a triple $(\mu^{(v)}, f^{(v)}, g^{(v)})$ consisting of a distribution $\mu^{(v)}$ on the inputs $\mathbf{x} \in \mathbb{R}^d$, a representation function $f^{(v)} : \mathbb{R}^d \rightarrow \mathbb{R}^{d'}$ where $d' \leq d$, and a stochastic labeling function $g^{(v)} : \mathbb{R}^{d'} \rightarrow \mathcal{Y}$ mapping the representation space to label space \mathcal{Y} . We denote the unseen domain by $(\mu^{(u)}, f^{(u)}, g^{(u)})$ and the S seen domains by $(\mu^{(s)}, f^{(s)}, g^{(s)})$, $s = 1, \dots, S$.

Let $\mathcal{F} = \{f|f : \mathbb{R}^d \rightarrow \mathbb{R}^{d'}\}$ be a set of *representation functions*, $\mathcal{G} = \{g|g : \mathbb{R}^{d'} \rightarrow \mathcal{Y}\}$ a set of *stochastic labeling functions*, and $\mathcal{H} := \mathcal{G} \circ \mathcal{F}$ the set of *hypothesis* $h : \mathbb{R}^d \rightarrow \mathcal{Y}$ obtained by composing each $g \in \mathcal{G}$ with each $f \in \mathcal{F}$, i.e., $h = g \circ f$.

Define the risk of using a hypothesis h in domain v by:

$$R^{(v)}(h) := \mathbb{E}_{\mathbf{x} \sim \mu^{(v)}} [\ell(h(\mathbf{x}), h^{(v)}(\mathbf{x}))] \quad (1)$$

where $\mathbb{E}[\cdot]$ denotes expectation, $h^{(v)} = g^{(v)} \circ f^{(v)}$, and $\ell(\cdot, \cdot)$ is a loss function. We make the following modeling assumptions:

A1: $\ell(\cdot, \cdot)$ is non-negative, symmetric, bounded by a finite positive number L , and satisfies the triangle inequality.

A2: The representation function f is invertible when restricted to the intrinsically low-dimensional data manifold.

Assumption A1 can be easily satisfied by any metric or norm truncated by a finite positive number. Concretely, if $d(a, b)$ is a metric, potentially unbounded like Mean Squared Error (MSE), then $loss(a, b) := \min(L, d(a, b))$ satisfies A1. In contrast to our requirements, the loss function in [Redko et al., 2017] is supposed to be convex, symmetric, bounded, obeying the triangle inequality, and satisfying a specific form, while the loss function in [Shen et al., 2018] required to be Lipschitz with respect to the hypothesis due to the use of Wasserstein-1 distance.

Assumption A2 can be explained by the manifold hypothesis that real-world data like images lie in a low-dimensional manifold within a high-dimensional space, which is also the basis of most dimension-reducing mappings such as those based on classical PCA, auto-encoders, etc.. Thus, the dimensional-reducing mapping f can be exactly invertible or nearly so when restricted to an intrinsically low-dimensional data manifold embedded within the high-dimensional ambient space. The same phenomena and its application can also be seen in compressive sampling. For example, it is possible to recover a sparse high dimensional signal which belongs to the union of sub-spaces - a low-dimensional manifold, from a compressed low-dimensional linear mapping. Additionally, note that the success of Generative Adversarial Networks (GAN) [Goodfellow et al., 2014] is also based on transforming a low-dimensional Gaussian to a distribution on an ambient space of high dimension. In practice, invertibility can be approximately achieved if there exists a reconstruction map with a sufficiently low reconstruction error or if the mutual information between the input and its representation is large enough. Indeed, our ablation study in Section 4.1 confirms the importance of imposing the invertibility condition in practical algorithms. Finally, although the results in this paper mainly rely on the assumption of invertible maps, we show that this assumption can be relaxed to be nearly invertible with more constraints added, as shown in Supplementary B.2.

2.1 Bounds Relating Seen and Unseen Domain Risks

We begin by considering a single seen domain. Lemma 1 below upper bounds the risk $R^{(u)}(h)$ of a hypothesis $h = g \circ f$ in the unseen domain u by three terms: (1) its risk $R^{(s)}(h)$ in a *single* seen domain s , (2) the L^1 distance between the distributions of the *representations* of data from the seen and unseen domain, and (3) a third term $\sigma^{(u,s)}$ that is free of h and is intrinsic to the domains and the loss function. We use the notation $f_{\#}\mu^{(v)}$ to denote the pushforward of distribution of $\mu^{(v)}$, i.e., the distribution of $f(\mathbf{x})$ with $\mathbf{x} \sim \mu^{(v)}$.

Lemma 1. *For any hypothesis $h \in \mathcal{H}$,*

$$R^{(u)}(h) \leq R^{(s)}(h) + L \|f_{\#}\mu^{(u)} - f_{\#}\mu^{(s)}\|_1 + \sigma^{(u,s)}$$

where $\|f_{\#}\mu^{(u)} - f_{\#}\mu^{(s)}\|_1 = \int |f_{\#}\mu^{(u)} - f_{\#}\mu^{(s)}| d\mathbf{x}$ denotes the L^1 distance between $(f_{\#}\mu^{(u)}, f_{\#}\mu^{(s)})$ and

$$\sigma^{(u,s)} := \min \left\{ \mathbb{E}_{\mathbf{x} \sim \mu^{(u)}} [\ell(h^{(u)}(\mathbf{x}), h^{(s)}(\mathbf{x}))], \mathbb{E}_{\mathbf{x} \sim \mu^{(s)}} [\ell(h^{(u)}(\mathbf{x}), h^{(s)}(\mathbf{x}))] \right\}. \quad (2)$$

Proof. Please see Supplementary B.1. □

The proposed upper bound in Lemma 1 requires f to be invertible. Particularly, the invertibility assumption is employed in the proof of Lemma 1, Eq. (22), Supplementary B.1. This condition can be relaxed to be nearly invertible as discussed in Supplementary B.2, and implemented by minimizing reconstruction loss or maximizing the mutual information between representation and the input data as discussed in Section 2.2.

In typical applications of DG, training data from multiple seen domains are available which can be mixed together in myriad ways. Lemma 2 below therefore extends Lemma 1 to a convex combination of distributions of seen domains.

Lemma 2. *For all convex weights $\lambda^{(1)}, \lambda^{(2)}, \dots, \lambda^{(S)}$ (nonnegative and summing to one) and any hypothesis $h \in \mathcal{H}$,*

$$R^{(u)}(h) \leq \sum_{s=1}^S \lambda^{(s)} R^{(s)}(h) + L \sum_{s=1}^S \lambda^{(s)} \|f_{\#}\mu^{(u)} - f_{\#}\mu^{(s)}\|_1 + \sum_{s=1}^S \lambda^{(s)} \sigma^{(u,s)}.$$

Proof. This follows immediately by taking the convex combination of the bound given by Lemma 1 over the seen domains. □

The upper bound is based on the L^1 distances between the pushforwards of seen and unseen distributions. Estimating L^1 distances accurately from samples is well-known to be hard [Batu et al., 2000, Ben-David et al., 2010, Kifer et al., 2004]. To overcome this practical limitation, we upper bound the L^1 distance by the Wasserstein-2 distance under additional regularity assumptions on the pushforwards.

Definition 1. [Polyanskiy and Wu, 2016] *A probability distribution on \mathbb{R}^d is called (c_1, c_2) -regular, with $c_1, c_2 \geq 0$, if it is absolutely continuous with respect to the Lebesgue measure with a differentiable density $p(\mathbf{x})$ such that*

$$\forall \mathbf{x} \in \mathbb{R}^d, \quad \|\nabla \log_2 p(\mathbf{x})\|_2 \leq c_1 \|\mathbf{x}\|_2 + c_2,$$

where ∇ denotes the gradient and $\|\cdot\|_2$ denotes the standard Euclidean norm.

Lemma 3. *If μ and ν are (c_1, c_2) -regular, then*

$$\|\mu - \nu\|_1 \leq \sqrt{c_1 \left(\sqrt{\mathbb{E}_{\mathbf{u} \sim \mu} [\|\mathbf{u}\|_2^2]} + \sqrt{\mathbb{E}_{\mathbf{v} \sim \nu} [\|\mathbf{v}\|_2^2]} \right) + 2c_2} \times \sqrt{W_2(\mu, \nu)} \quad (3)$$

where, $W_p(\mu, \nu)$ denotes the Wasserstein- p metric [Peyré and Cuturi, 2019, Santambrogio, 2015, Villani, 2003] defined as,

$$W_p(\mu, \nu) := \min_{\pi \in \Pi(\mu, \nu)} (\mathbb{E}_{(\mathbf{u}, \mathbf{v}) \sim \pi} [\|\mathbf{u} - \mathbf{v}\|_2^p])^{1/p}$$

where $\Pi(\mu, \nu)$ is the set of joint distributions with marginals μ and ν .

Proof. Please see Supplementary B.3. □

One may ask: what conditions guarantee the regularity of the pushforward distributions? Proposition 2 and Proposition 3 in [Polyanskiy and Wu, 2016] show that any distribution ν for which $\mathbb{E}_{\mathbf{v} \sim \nu} \|\mathbf{v}\|_2$ is finite becomes regular when convolved with any regular distribution, including the Gaussian distribution. Since convolution of distributions corresponds to addition of independent random vectors having those distributions, in practice it is always possible to make the pushforwards regular by adding a small amount of independent spherical Gaussian noise in representation space.

Combining Lemma 2, Lemma 3, and Jensen’s inequality, we obtain our main result:

Theorem 1. *If $f_{\#}\mu^{(s)}$, $s = 1, 2, \dots, S$, and $f_{\#}\mu^{(u)}$ are all (c_1, c_2) -regular, then for all convex weights $\lambda^{(1)}, \lambda^{(2)}, \dots, \lambda^{(S)}$ and any hypothesis $h \in \mathcal{H}$,*

$$R^{(u)}(h) \leq \sum_{s=1}^S \lambda^{(s)} R^{(s)}(h) + LC \left[\sum_{s=1}^S \lambda^{(s)} \mathcal{W}_2^2(f_{\#}\mu^{(u)}, f_{\#}\mu^{(s)}) \right]^{1/4} + \sum_{s=1}^S \lambda^{(s)} \sigma^{(u,s)} \quad (4)$$

where

$$C = \max_s \sqrt{c_1 \left(\sqrt{\mathbb{E}_{\mathbf{x} \sim \mu^{(u)}} [\|f(\mathbf{x})\|^2]} + \sqrt{\mathbb{E}_{\mathbf{x} \sim \mu^{(s)}} [\|f(\mathbf{x})\|^2]} \right) + 2c_2}.$$

Proof. Please see Supplementary B.4. □

It is worth noting that the third term $\sum_{s=1}^S \lambda^{(s)} \sigma^{(u,s)}$ in the upper bound of Theorem 1 is independent from both the representation map f and the labeling function g that contrasts to the previous results in [Ben-David et al., 2007], please see our detailed analysis in Supplementary A.1. In addition, one may find the form of the upper bound derived above shares some similarities with Lemma 1 in [Redko et al., 2017] and Theorem 1 in [Shen et al., 2018], for example, all of them introduce Wasserstein distance between domain distributions. But the content is indeed different from previous work based on the following key points.

1. Our upper bound is constructed in the *representation* space, not in the data (ambient) space, which provides a theoretical justification for the risk of unseen domain when decomposing the hypothesis into a representation mapping and a labeling function. This is also consistent with the algorithm implementation in practice.
2. The loss function in [Redko et al., 2017] is assumed to be convex, symmetric, bounded, obeying the triangle inequality, and satisfying a specific form, while in [Shen et al., 2018], it is required to be Lipschitz with respect to the hypothesis due to the use of Wasserstein-1 distance. With less constraints posed on the loss function, we only assume it is symmetric, bounded, and satisfies triangle inequality.
3. The bounds in Lemma 1 of [Redko et al., 2017] and Theorem 1 of [Shen et al., 2018] are controlled by the Wasserstein-1 distance while our upper bound is managed by the square-root of the Wasserstein-2 distance. There are regimes where one bound is tighter than the other. Please see the detailed analysis in Supplementary A.2.

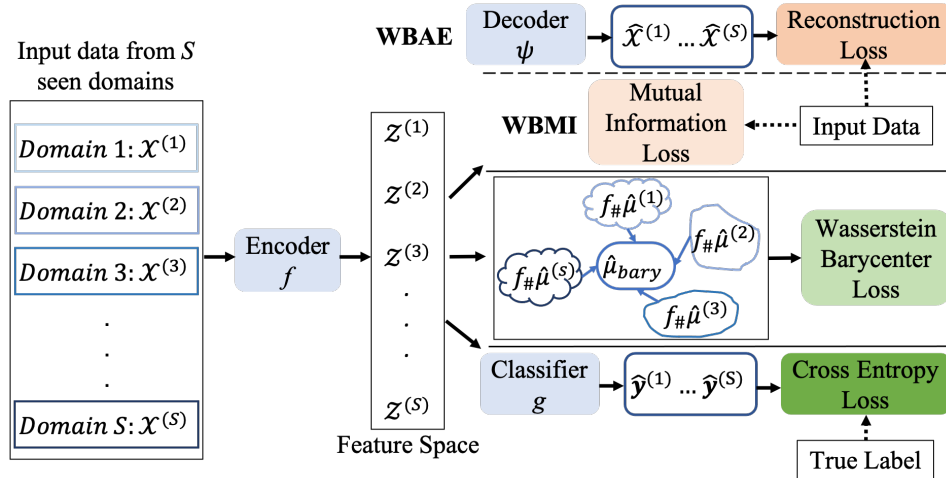


Figure 1: An Overview of the Proposed Algorithms. On the top branch, two sub-branches refer to either choosing WBAE or WBMI.

2.2 Proposed Methods

The upper bound in Theorem 1 is composed of three terms. Since the third term is independent of both the representation function f and the labeling function g , we can mainly focus on designing f and g to minimize the first and second terms. Following previous work [Albuquerque et al., 2019, Ben-David et al., 2007, 2010], we optimize the first term by training f together with g using a standard cross-entropy (CE) loss, such that the empirical risk on seen domains is minimized. The loss function can be written as:

$$\mathcal{L}_c(f, g) = \min_{f, g} \sum_{s=1}^S \mathbb{E}_{\mathbf{x} \sim \mu^{(s)}} [\text{CE}(h^{(s)}(\mathbf{x}), g(f(\mathbf{x})))] \quad (5)$$

where $\text{CE}(h^{(s)}(\mathbf{x}), g(f(\mathbf{x})))$ denotes the cross entropy (CE) loss between the output of classifier and the ground-truth label of seen domain s .

The unavailability of the data distribution from unseen domain hinders the direct optimization of the second term in Eq. (4). To address this issue, we propose to use the Wasserstein-2 barycenter of the representation distributions from seen domains as a proxy for the representation distribution of the unseen domain, leading to the following loss term:

$$\mathcal{L}_{bary}(f) := \min_{\mu} \sum_{s=1}^S \frac{1}{S} W_2^2(\mu, f_{\#}\mu^{(s)}). \quad (6)$$

In contrast to the previous Wasserstein distance-based method in [Zhou et al., 2021a] where pairwise Wasserstein distance loss is employed, we motivate the Wasserstein barycenter loss from Eq. (4). One can easily observe that the second term in Eq. (4) has a similar form with the barycenter loss in Eq. (6). Without any extra information about the distribution of the unseen domain, we assume that the pushforward of unseen distribution $f_{\#}\mu^{(u)}$ lies not far from the Wasserstein-2 barycenter formed by the pushforward of the seen distributions $\{f_{\#}\mu^{(s)}\}_{s=1}^S$, and thus can be represented by the

Wasserstein-2 barycenter term. Under such assumption, optimizing the barycenter loss will lead to the minimization of the proposed upper bound. Further, note that from the definition in Eq. (6), computing barycenter loss requires computing S Wasserstein distances in contrast to $S(S-1)/2$ when using pairwise Wasserstein distances. Even though the motivation of Wasserstein barycenter is somewhat heuristic, the importance of the use of Wasserstein barycenter loss is proven in our ablation study in Section 4.1.

Furthermore, to incorporate our assumption that f is manifold restricted invertible, we empirically explore two methods to enforce this constraint, i.e., reconstruction-based method and mutual information-based method.

The first method is inspired by the structure of auto-encoder, which is commonly used for dimension reduction and data denoising [Wang et al., 2016, Vincent et al., 2008]. We adopt the encoder-decoder structure and introduce reconstruction loss to approximate the invertibility constraint. More specifically, a decoder $\psi : \mathbb{R}^{d'} \rightarrow \mathbb{R}^d$ is adopted, leading to the following loss term:

$$\mathbf{L}_r(f, \psi) := \min_{f, \psi} \sum_{s=1}^S \mathbb{E}_{\mathbf{x} \sim \mu^{(s)}} \|\mathbf{x} - \psi(f(\mathbf{x}))\|^2. \quad (7)$$

The other method is motivated by the manifold hypothesis and rate-distortion theory. Particularly, we propose to use mutual information (MI) $I(\mathbf{X}^{(s)}; f(\mathbf{X}^{(s)}))$ [Cover, 1999] between the input of seen domain s and its (noisy) representation as a measure of the invertibility of f . The MI quantifies the dependence between $\mathbf{X}^{(s)}$ and $f(\mathbf{X}^{(s)})$, the larger the mutual information is, the more statistically dependent between the input and its representation. In other words, if f fails to achieve the invertibility, the MI term will be small due to the loss of information after representation mapping. This gives rise to the following term, note we put a negative sign for minimization:

$$\min_f - \sum_{s=1}^S I(\mathbf{X}^{(s)}; f(\mathbf{X}^{(s)})). \quad (8)$$

From the previous analysis, to enforce the invertibility constraint while balancing the other objectives, we propose two objective functions in Eq. (9) and Eq. (10) which can be interpreted as a Lagrangian approach:

$$\arg \min_{f, g, \psi} \mathbf{L}_c(f, g) + \alpha \mathbf{L}_{bary}(f) + \beta \mathbf{L}_r(f, \psi) \quad (9)$$

and

$$\arg \min_{f, g} \mathbf{L}_c(f, g) + \alpha \mathbf{L}_{bary}(f) - \beta \sum_{s=1}^S I(\mathbf{X}^{(s)}; f(\mathbf{X}^{(s)})) \quad (10)$$

where $\alpha, \beta > 0$ are hyperparameters. It can be seen that the proposed upper bound is extensively incorporated by our objective functions in Eq. (9) and (10). Particularly, the first term in both objective functions aims to determine a good classifier g together with a representation mapping f by minimizing the training error, which corresponds to the first term of the upper bound in Eq. (4). The second term in Eq. (9) and (10) minimizes the discrepancy between seen and unseen domains, contributing to a domain-invariant mapping. Motivated by the proposed upper bound, we treat the

Wasserstein-2 barycenter as a proxy of the representation distribution of the unseen domain. In this way, it shares the same form with the second term in the upper bound, making it possible to minimize the discrepancy of different domains directly. Noting that though L_{bary} itself requires solving an optimization problem, we leverage fast computation methods, which is also discussed in Section 3, to directly estimate this loss without invoking the Kantorovich-Rubenstein dual characterization of Wasserstein distances [Villani, 2003, Santambrogio, 2015]. This avoids solving for a min-max type problem that is often plagued with unstable numerical dynamics. Moreover, according to the manifold invertibility assumption required in Theorem 1, we add the third term in Eq. (9) and (10).

3 ALGORITHMS

Based on the loss functions designed above, we propose algorithms that aim to learn domain-invariant but task-sensitive representations. Depending on how the invertibility criteria is dealt with, we design two different algorithms: Wasserstein Barycenter loss with Auto-Encoder (WBAE) and Wasserstein Barycenter loss with Mutual Information (WBMI) which are combined in Algorithm 1. WBAE adopts the auto-encoder structure to maintain the invertibility, while WBMI adds a mutual information term in the loss function for enforcing it. An overview of the proposed methods is shown in Figure 1.

Both algorithms involve calculating Wasserstein-2 barycenter and its supporting points. Here we use an off-the-shelf python package [Flamary et al., 2021] that implements a free-support Wasserstein barycenter algorithm described in [Cuturi and Doucet, 2014]. This algorithm is executed in the primal domain and avoids the use of the dual form of Wasserstein distances, which otherwise would turn the problem into an adversarial (min-max) type setting that we want to avoid due to its instability. The barycenter loss is approximated via an average Sinkhorn divergence [Feydy et al., 2019] between the seen domains and the estimated barycenter. Sinkhorn divergence is an unbiased proxy for the Wasserstein distance, which leverages entropic regularization [Cuturi, 2013] for computational efficiency, thereby allowing for integrating automatic differentiation with GPU computation. We adopt the implementation in [Feydy et al., 2019] to our algorithm for a fast gradient computation and denote it as $Sinkhorn_\epsilon$ in Algorithm 1, where ϵ is the entropic regularization term.

For WBAE method, we use an encoder f and a decoder ψ , which are parameterized by θ_e and θ_d , for feature extraction and enforcing the invertibility. Here $\mathcal{X}^{(s)}$ is denoted as a set of samples from domain s with empirical distribution $\hat{\mu}^{(s)}$ with $\mathbf{x}_i^{(s)}$ as one of its element. The corresponding label set of $\mathcal{X}^{(s)}$ is $\mathbf{y}^{(s)}$, where $\mathbf{y}^{(s)} := \{y_i^{(s)}\}$ with $y_i^{(s)}$ is the label for sample $\mathbf{x}_i^{(s)}$. The extracted feature $\mathbf{z}_i^{(s)} = f_{\theta_e}(\mathbf{x}_i^{(s)})$ in set $\mathcal{Z}^{(s)}$ is under the empirical distribution of $f_{\#}\hat{\mu}^{(s)}$. The decoder takes the extracted features as input and outputs the reconstructions as $\psi_{\theta_d}(\mathbf{z}_i^{(s)})$ for domain s . The classifier g , which is parameterized by θ_c is applied to the extracted features for label prediction. As a surrogate of the decoder ψ_{θ_d} , WBMI maximizes the mutual information between the input data and the extracted feature as an objective to obligate the invertibility. Since mutual information is intractable when the distribution is unknown, we adopt the Mutual Information Gradient Estimation (MIGE) [Wen et al., 2020] framework to estimate the gradient of mutual information between the distribution of the input data and the extracted feature. Moreover, to avoid the mutual information going to infinity, we add a

small noise to the extracted feature.

Algorithm 1 Wasserstein Barycenter Loss with Auto-Encoder/ Mutual Information (WBAE/WBMI)

Input: Data from S seen domains, batch size m , learning rate η , parameters $\alpha, \beta, \epsilon, \delta$. **Output:** Encoder f_{θ_e} , decoder ψ_{θ_d} , classifier g_{θ_c}

```

1: while training is not end do
2:   Randomly chose  $m^{(s)} = \frac{m}{S}$  samples from each domain, denoted as  $\mathcal{X}^{(s)} := \{\mathbf{x}_i^{(s)}\}_{i=1}^{m^{(s)}} \sim \hat{\mu}^{(s)}$  and
    $\mathbf{y}^{(s)} := \{y_i^{(s)}\}_{i=1}^{m^{(s)}}$ 
3:   for  $s = 1 : S$  and  $i = 1 : m^{(s)}$  do
4:      $\mathbf{z}_i^{(s)} \leftarrow f_{\theta_e}(\mathbf{x}_i^{(s)})$  with set  $\mathcal{Z}^{(s)} \sim f_{\#}\hat{\mu}^{(s)}$ 
5:     if WBMI then
6:        $\mathcal{Z}_{noise}^{(s)} \leftarrow \mathcal{Z}^{(s)} + \delta\mathcal{N}(0, 1)$ 
7:     end if
8:   end for
9:   Calculate the Wasserstein barycenter  $\hat{\mu}_{bary}$  of  $\{f_{\#}\hat{\mu}^{(s)}\}_{s=1}^S$  and its supporting points with  $f_{\theta_e}$ 
   detached from automatic backpropagation
10:   $\mathcal{L}_{wb} = \frac{1}{S} \sum_{s=1}^S Sinkhorn_{\epsilon}(\hat{\mu}_{bary}, f_{\#}\hat{\mu}^{(s)})$ 
11:   $\mathcal{L}_c = -\frac{1}{m} \sum_{s=1}^S \sum_{i=1}^{m^{(s)}} y_i^s \log p(g_{\theta_c}(f_{\theta_e}(\mathbf{x}_i^{(s)})))$ 
12:  if WBAE then
13:     $\mathcal{L}_r = \frac{1}{m} \sum_{s=1}^S \sum_{i=1}^{m^{(s)}} \|\mathbf{x}_i^{(s)} - \psi_{\theta_d}(\mathbf{z}_i^{(s)})\|_2^2$ 
14:     $\theta_c = \theta_c - \eta \nabla_{\theta_c} \mathcal{L}_c$ ,  $\theta_d = \theta_d - \eta \nabla_{\theta_d} \mathcal{L}_r$ 
15:     $\mathcal{L} = \mathcal{L}_c + \alpha \mathcal{L}_{wb} + \beta \mathcal{L}_r$ 
16:     $\theta_e = \theta_e - \eta \nabla_{\theta_e} \mathcal{L}$ 
17:  else if WBMI then
18:    Estimate the gradient of mutual information between the empirical distribution of  $\{\mathcal{X}^{(s)}\}_{s=1}^S$ 
    and  $\{\mathcal{Z}_{noise}^{(s)}\}_{s=1}^S$  via MIGE, denoted as  $\nabla_{\theta_e} \mathcal{L}_i$ 
19:     $\theta_c = \theta_c - \eta \nabla_{\theta_c} \mathcal{L}_c$ 
20:     $\theta_e = \theta_e - \eta(\alpha \nabla_{\theta_e} \mathcal{L}_{wb} - \beta \nabla_{\theta_e} \mathcal{L}_i)$ 
21:  end if
22: end while

```

4 EXPERIMENTS AND RESULTS

We evaluate the proposed methods on three widely used DG datasets: Office-Caltech, Office-Home, and Rotated MNIST. Due to the space constraints, here only experiments and results on Office-Caltech and Office-Home datasets are presented. The results for Rotated MNIST, a thorough description for all datasets and implementation details for comparison methods can be found in Supplementary C.

Office-Caltech: Office-Caltech [Gong et al., 2012] dataset consists of 2533 images from 4 different domains: Amazon (A), Caltech-256 (C), DSLR (D) and Webcam (W). We use the 4096 dimensional DeCAF₆ features [Donahue et al., 2014] as input.

Office-Home: Office-Home [Venkateswara et al., 2017] dataset is a larger dataset with 15,500 images from 4 different domains: Artistic images (A), Clip Art (C), Product images (P), and Real-World (R). Here we extract ResNet-50 deep features from each domain as input. Detail information about the process of ResNet-50 deep feature extraction can be found in Supplementary C.1.

Methods Compared: We compare our methods with the following algorithms: Empirical Risk Minimization (ERM), Meta Learning Domain Generalization (MLDG) [Li et al., 2018a], Domain Adversarial Neural Network (DANN) [Ganin et al., 2016], and Maximum Mean Discrepancy Adversarial Autoencoder (MMD-AAE) [Li et al., 2018b]. The description and implementation details of the comparison methods can be found in Supplementary C.2.

Training Procedure: The model used for all methods can be found in Supplementary C.3. We follow the leave-one-domain-out protocol in [Dou et al., 2019] to conduct DG tasks. Data from each domain is randomly split into training and validation sets in the proportion of 80% and 20%, respectively. During training, we aggregated the training/validation from each seen domain to form the overall training/validation set. For hyper-parameters tuning, we perform a grid search over a range [0.01,10] with a \log_{10} scale and choose parameters that produce the lowest averaged validation loss over all DG tasks. After fixing the hyper-parameters, we re-train the model and select the one with the lowest validation loss to generate the final classification accuracy on the test domain data. This hyper-parameter tuning and model selection strategy is applied to all models that we evaluate. Models are trained for 300 epochs using the Adam optimizer [Kingma and Ba, 2015] with the learning rate of 5×10^{-5} for both datasets.

For Office-Caltech dataset, the batch size of the proposed methods m is set to 150, the values of ϵ for the Sinkhorn loss and δ (line 6, Algorithm 1) for Gaussian noise are empirically chosen without tuning and fixed at 0.5 and 0.1 for all tasks, and the (α, β) pair is set to (0.01, 10) for WBAE and (0.1, 0.01) for WBMI. For Office-Home dataset, the batch size of the proposed methods m is doubled, and the (α, β) pair is set to (0.01, 0.1) for WBAE and (0.1, 0.1) for WBMI, respectively. All the other settings are the same as that for the Office-Caltech dataset.

We use Nvidia-tesla p100 16 GB GPU for computation and one round of training (300 epochs) will take half an hour for the proposed methods. The above procedure is repeated five times for each model and the average accuracy and standard deviation values are reported.

Results: Results for the Office-Caltech dataset are shown in Table 1. Both the proposed algorithms have very similar performance with only modest improvements over all the comparison methods. The comparable performance of all methods can be attributed to the small size of the dataset and the limited diversity between domains. However, when we examine results for the larger and more challenging Office-Home dataset, our methods outperform the comparison methods which include DA method, meta-learning based method, and adversarial DG method, in all four tasks as shown in Table 2. Specifically, the WBAE outperforms all the comparison methods by at least 1.4% on average. A larger performance improvement is observed with our WBMI method, boosting the classification accuracy by at least 4.4% on average compared to all the comparison methods and by at least 4.1%, 4.3%, 3.8% and 3.8% on each task. A similar results can be observed for Rotated MNIST dataset, where WBAE and WBMI surpass all the compared methods as shown in Supplementary C.4.

Table 1: Performance on Office-Caltech Dataset

| Unseen | A | C | D | W | Avg |
|---------|-----------------------|-----------------------|-----------------------|-----------------------|-----------------------|
| ERM | 90.8 \pm 0.9 | 81.8 \pm 1.8 | 96.4 \pm 1.0 | 88.4 \pm 1.5 | 89.4 \pm 1.4 |
| DANN | 91.1 \pm 0.4 | 83.2 \pm 1.1 | 96.7 \pm 2.2 | 90.4 \pm 1.8 | 90.4 \pm 1.5 |
| MMD-AAE | 90.9 \pm 0.6 | 82.5 \pm 1.5 | 97.6 \pm 0.8 | 93.7 \pm 1.4 | 91.2 \pm 1.1 |
| MLDG | 90.3 \pm 0.6 | 82.8 \pm 0.9 | 98.3 \pm 1.1 | 93.8 \pm 1.5 | 91.3 \pm 1.1 |
| WBAE | 91.3 \pm 0.5 | 84.1 \pm 1.0 | 98.5 \pm 0.3 | 93.4 \pm 2.0 | 91.8 \pm 1.2 |
| WBMI | 91.9 \pm 0.7 | 84.4 \pm 0.4 | 98.1 \pm 1.2 | 92.9 \pm 1.4 | 91.8 \pm 1.0 |

Table 2: Performance on Office-Home Dataset

| Unseen | A | C | P | R | Avg |
|---------|-----------------------|-----------------------|-----------------------|-----------------------|-----------------------|
| ERM | 54.9 \pm 0.6 | 42.1 \pm 0.4 | 70.9 \pm 0.3 | 73.1 \pm 0.3 | 60.2 \pm 0.5 |
| DANN | 56.9 \pm 0.2 | 43.2 \pm 1.2 | 70.6 \pm 0.4 | 73.4 \pm 0.2 | 61.0 \pm 0.7 |
| MMD-AAE | 55.4 \pm 0.2 | 44.0 \pm 0.5 | 70.6 \pm 0.4 | 73.8 \pm 0.2 | 60.9 \pm 0.3 |
| MLDG | 55.1 \pm 0.5 | 43.1 \pm 0.7 | 70.4 \pm 0.4 | 73.7 \pm 0.1 | 60.6 \pm 0.4 |
| WBAE | 57.0 \pm 0.5 | 44.3 \pm 1.3 | 73.0 \pm 0.2 | 75.2 \pm 0.5 | 62.4 \pm 0.8 |
| WBMI | 61.0 \pm 0.5 | 48.3 \pm 0.6 | 74.7 \pm 0.5 | 77.6 \pm 0.3 | 65.4 \pm 0.5 |

4.1 Ablation Study

To study the impact of different components of the total loss function, we conduct a full ablation study for the WBAE method and a partial one for WBMI method on both datasets. In particular, we consider the following variants of our method: (1) WBAE without Wasserstein barycenter loss, denoted as WBAE- L_{wb} ; (2) WBAE without reconstruction loss, denoted as WBAE- L_r , this variant can also be viewed as WBMI method without mutual information loss, so we also denote it as WBMI- L_i ; (3) original WBAE method with all the loss components, denoted as WBAE; (4) original WBMI method with all the loss components denotes as WBMI. During the experiment, we remove the decoder part for WBAE- L_r and re-run all the experiments using the same model architectures, parameter tuning and validation process.

From Table 3 and Table 4, we find that removing L_r/L_i from WBAE/WBMI model leads to a decrease in the accuracy of around 0.1%/0.1% for Office-Caltech dataset and 0.3%/3.3% for Office-Home dataset. The performance deterioration can be more clearly observed when omitting L_{wb} for WBAE model, leading to a drop of around 0.9% for Office-Caltech dataset and 2.1% for Office-Home dataset. More interestingly, we observe a 3% improvement in accuracy when replacing the reconstruction loss L_r in WBAE with the mutual information loss for Office-Home dataset.

Table 3: Ablation Study for Office-Caltech Dataset

| Unseen | ERM | WBAE- L_{wb} | WBAE- L_r WBMI- L_i | WBAE | WBMI |
|---------|----------------|----------------|----------------------------------|----------------------------------|----------------------------------|
| A | 90.8 ± 0.9 | 90.5 ± 0.7 | 91.3 ± 0.7 | 91.3 ± 0.5 | 91.9 ± 0.7 |
| C | 81.8 ± 1.8 | 82.2 ± 0.7 | 83.8 ± 0.9 | 84.1 ± 1.0 | 84.4 ± 0.4 |
| D | 96.4 ± 1.0 | 98.1 ± 0.9 | 98.7 ± 0.6 | 98.5 ± 0.3 | 98.1 ± 1.2 |
| W | 88.4 ± 1.5 | 92.5 ± 1.7 | 92.9 ± 1.7 | 93.4 ± 2.0 | 92.9 ± 1.4 |
| Average | 89.4 ± 1.4 | 90.9 ± 1.1 | 91.7 ± 1.1 | 91.8 ± 1.2 | 91.8 ± 1.0 |

Table 4: Ablation Study for Office-Home Dataset

| Unseen | ERM | WBAE- L_{wb} | WBAE- L_r WBMI- L_i | WBAE | WBMI |
|---------|----------------|----------------|----------------------------|----------------|----------------------------------|
| A | 54.9 ± 0.6 | 54.4 ± 0.7 | 56.3 ± 0.5 | 57.0 ± 0.5 | 61.0 ± 0.5 |
| C | 42.1 ± 0.4 | 43.1 ± 0.6 | 44.2 ± 0.9 | 44.3 ± 1.3 | 48.3 ± 0.6 |
| P | 70.9 ± 0.3 | 70.3 ± 0.3 | 72.9 ± 0.7 | 73.0 ± 0.2 | 74.7 ± 0.5 |
| R | 73.1 ± 0.3 | 73.2 ± 0.5 | 75.1 ± 0.3 | 75.2 ± 0.5 | 77.6 ± 0.3 |
| Average | 60.2 ± 0.5 | 60.3 ± 0.5 | 62.1 ± 0.7 | 62.4 ± 0.8 | 65.4 ± 0.5 |

This ablation study demonstrates the importance of the Wasserstein barycenter loss and also stresses the key role of the invertibility of the representation mapping. This is reflected in the performance of WBMI in achieving the best results overall, which also indicates that the use of auto-encoder may be more limited than using mutual information as a criteria. On the other hand, the estimation of the gradient for mutual information may not be accurate in higher dimensions, which is one limitation of the proposed WBMI method.

5 CONCLUSION AND FUTURE WORK

We revisited the theory and methods for DG and provided a new upper bound for the risk of unseen domain. Our analysis could be potentially tightened towards understanding minimal regularity conditions on the distribution and the loss functions that can yield better bounds or a family of bounds adapted to different situations. In terms of algorithms and numerical implementation, we note that our methods, although numerically stable and have better accuracy compared to adversarial and other related approaches, can be computationally expensive. This cost is primarily driven by the need to

reliably estimate the Wasserstein-2 barycenter, which is known to require a large number of samples in high dimensions [Korotin et al., 2021]. To alleviate this, one can employ the recently proposed large scale barycenter and mapping estimators [Fan et al., 2020]. It is to be noted that using adversarial approaches also suffer from the same sample complexity issues in order to reliably estimate the domain discrepancy in the representation space. The gradient estimation of mutual information is also known to degrade in higher dimensions and one can leverage some recent advances made to alleviate this issue [Belghazi et al., 2018, Wen et al., 2020].

References

- H. Ajakan, P. Germain, H. Larochelle, F. Laviolette, and M. Marchand. Domain-adversarial neural networks. *arXiv preprint arXiv:1412.4446*, 2014.
- I. Albuquerque, J. Monteiro, M. Darvishi, T. H. Falk, and I. Mitliagkas. Generalizing to unseen domains via distribution matching. *arXiv preprint arXiv:1911.00804*, 2019.
- T. Batu, L. Fortnow, R. Rubinfeld, W. D. Smith, and P. White. Testing that distributions are close. In *Proceedings 41st Annual Symposium on Foundations of Computer Science*, pages 259–269. IEEE, 2000.
- M. I. Belghazi, A. Baratin, S. Rajeshwar, S. Ozair, Y. Bengio, A. Courville, and D. Hjelm. Mutual information neural estimation. In *International Conference on Machine Learning*, pages 531–540. PMLR, 2018.
- S. Ben-David, J. Blitzer, K. Crammer, F. Pereira, et al. Analysis of representations for domain adaptation. *Advances in neural information processing systems*, 19:137, 2007.
- S. Ben-David, J. Blitzer, K. Crammer, A. Kulesza, F. Pereira, and J. W. Vaughan. A theory of learning from different domains. *Machine learning*, 79(1):151–175, 2010.
- D. Berend, P. Harremoës, and A. Kontorovich. Minimum kl-divergence on complements of l_1 balls. *IEEE Transactions on Information Theory*, 60(6):3172–3177, 2014. doi: 10.1109/TIT.2014.2301446.
- G. Blanchard, G. Lee, and C. Scott. Generalizing from several related classification tasks to a new unlabeled sample. *Advances in neural information processing systems*, 24:2178–2186, 2011.
- T. M. Cover. *Elements of information theory*. John Wiley & Sons, 1999.
- I. Csiszár and J. Körner. *Information theory: coding theorems for discrete memoryless systems*. Cambridge University Press, 2011.
- Y. Cui, Y. Xu, and D. Wu. Eeg-based driver drowsiness estimation using feature weighted episodic training. *IEEE transactions on neural systems and rehabilitation engineering*, 27(11):2263–2273, 2019.
- M. Cuturi. Sinkhorn distances: Lightspeed computation of optimal transport. *Advances in neural information processing systems*, 26:2292–2300, 2013.
- M. Cuturi and A. Doucet. Fast computation of wasserstein barycenters. In *International conference on machine learning*, pages 685–693. PMLR, 2014.
- J. Donahue, Y. Jia, O. Vinyals, J. Hoffman, N. Zhang, E. Tzeng, and T. Darrell. Decaf: A deep convolutional activation feature for generic visual recognition. In *International conference on machine learning*, pages 647–655. PMLR, 2014.

- Q. Dou, D. C. Castro, K. Kamnitsas, and B. Glocker. Domain generalization via model-agnostic learning of semantic features. *arXiv preprint arXiv:1910.13580*, 2019.
- J. Fan, A. Taghvaei, and Y. Chen. Scalable computations of wasserstein barycenter via input convex neural networks. *arXiv preprint arXiv:2007.04462*, 2020.
- J. Feydy, T. Séjourné, F.-X. Vialard, S.-i. Amari, A. Trounev, and G. Peyré. Interpolating between optimal transport and mmd using sinkhorn divergences. In *The 22nd International Conference on Artificial Intelligence and Statistics*, pages 2681–2690, 2019.
- R. Flamary, N. Courty, A. Gramfort, M. Z. Alaya, A. Boisbunon, S. Chambon, L. Chapel, A. Corenflos, K. Fatras, N. Fournier, L. Gautheron, N. T. Gayraud, H. Janati, A. Rakotomamonjy, I. Redko, A. Rolet, A. Schutz, V. Seguy, D. J. Sutherland, R. Tavenard, A. Tong, and T. Vayer. Pot: Python optimal transport. *Journal of Machine Learning Research*, 22(78):1–8, 2021. URL <http://jmlr.org/papers/v22/20-451.html>.
- Y. Ganin, E. Ustinova, H. Ajakan, P. Germain, H. Larochelle, F. Laviolette, M. Marchand, and V. Lempitsky. Domain-adversarial training of neural networks. *The journal of machine learning research*, 17(1):2096–2030, 2016.
- M. Ghifary, W. B. Kleijn, M. Zhang, and D. Balduzzi. Domain generalization for object recognition with multi-task autoencoders. In *Proceedings of the IEEE international conference on computer vision*, pages 2551–2559, 2015.
- B. Gong, Y. Shi, F. Sha, and K. Grauman. Geodesic flow kernel for unsupervised domain adaptation. In *2012 IEEE conference on computer vision and pattern recognition*, pages 2066–2073. IEEE, 2012.
- I. Goodfellow, J. Pouget-Abadie, M. Mirza, B. Xu, D. Warde-Farley, S. Ozair, A. Courville, and Y. Bengio. Generative adversarial nets. *Advances in neural information processing systems*, 27, 2014.
- I. Gulrajani and D. Lopez-Paz. In search of lost domain generalization. *arXiv preprint arXiv:2007.01434*, 2020.
- M. Ilse, J. M. Tomczak, C. Louizos, and M. Welling. Diva: Domain invariant variational autoencoders. In *Medical Imaging with Deep Learning*, pages 322–348. PMLR, 2020.
- D. Kifer, S. Ben-David, and J. Gehrke. Detecting change in data streams. In *VLDB*, volume 4, pages 180–191. Toronto, Canada, 2004.
- D. P. Kingma and J. Ba. Adam: A method for stochastic optimization. In Y. Bengio and Y. LeCun, editors, *3rd International Conference on Learning Representations, ICLR 2015, San Diego, CA, USA, May 7-9, 2015, Conference Track Proceedings*, 2015. URL <http://arxiv.org/abs/1412.6980>.
- A. Korotin, L. Li, J. Solomon, and E. Burnaev. Continuous wasserstein-2 barycenter estimation without minimax optimization. *arXiv preprint arXiv:2102.01752*, 2021.

- N. Lei, D. An, Y. Guo, K. Su, S. Liu, Z. Luo, S.-T. Yau, and X. Gu. A geometric understanding of deep learning. *Engineering*, 6(3):361–374, 2020. ISSN 2095-8099. doi: <https://doi.org/10.1016/j.eng.2019.09.010>. URL <https://www.sciencedirect.com/science/article/pii/S2095809919302279>.
- D. Li, Y. Yang, Y.-Z. Song, and T. M. Hospedales. Learning to generalize: Meta-learning for domain generalization. In *Thirty-Second AAAI Conference on Artificial Intelligence*, 2018a.
- H. Li, S. J. Pan, S. Wang, and A. C. Kot. Domain generalization with adversarial feature learning. In *Proceedings of the IEEE Conference on Computer Vision and Pattern Recognition*, pages 5400–5409, 2018b.
- B. Lyu, T. Pham, G. Blaney, Z. Haga, A. Sassaroli, S. Fantini, and S. Aeron. Domain adaptation for robust workload level alignment between sessions and subjects using fNIRS. *Journal of Biomedical Optics*, 26(2):1 – 21, 2021. doi: 10.1117/1.JBO.26.2.022908. URL <https://doi.org/10.1117/1.JBO.26.2.022908>.
- G. Peyré and M. Cuturi. Computational optimal transport. *Foundations and Trends in Machine Learning*, 11 (5-6):355–602, 2019.
- Y. Polyanskiy and Y. Wu. Wasserstein continuity of entropy and outer bounds for interference channels. *IEEE Transactions on Information Theory*, 62(7):3992–4002, 2016.
- I. Redko, A. Habrard, and M. Sebban. Theoretical analysis of domain adaptation with optimal transport. In *Joint European Conference on Machine Learning and Knowledge Discovery in Databases*, pages 737–753. Springer, 2017.
- I. Redko, E. Morvant, A. Habrard, M. Sebban, and Y. Bennani. A survey on domain adaptation theory: learning bounds and theoretical guarantees. *arXiv e-prints*, pages arXiv–2004, 2020.
- F. Santambrogio. *Optimal Transport for Applied Mathematicians: Calculus of Variations, PDEs and Modeling*. Springer, 2015.
- J. Shen, Y. Qu, W. Zhang, and Y. Yu. Wasserstein distance guided representation learning for domain adaptation. In *Thirty-Second AAAI Conference on Artificial Intelligence*, 2018.
- A. van den Oord, Y. Li, and O. Vinyals. Representation learning with contrastive predictive coding. *CoRR*, abs/1807.03748, 2018. URL <http://arxiv.org/abs/1807.03748>.
- H. Venkateswara, J. Eusebio, S. Chakraborty, and S. Panchanathan. Deep hashing network for unsupervised domain adaptation. In *Proceedings of the IEEE conference on computer vision and pattern recognition*, pages 5018–5027, 2017.
- C. Villani. *Topics in optimal transportation*. Number 58. American Mathematical Soc., 2003.
- P. Vincent, H. Larochelle, Y. Bengio, and P.-A. Manzagol. Extracting and composing robust features with denoising autoencoders. In *Proceedings of the 25th international conference on Machine learning*, pages 1096–1103, 2008.

- J. Wang, C. Lan, C. Liu, Y. Ouyang, and T. Qin. Generalizing to unseen domains: A survey on domain generalization. *arXiv e-prints*, pages arXiv–2103, 2021.
- Y. Wang, H. Yao, and S. Zhao. Auto-encoder based dimensionality reduction. *Neurocomputing*, 184: 232–242, 2016.
- L. Wen, Y. Zhou, L. He, M. Zhou, and Z. Xu. Mutual information gradient estimation for representation learning. *arXiv preprint arXiv:2005.01123*, 2020.
- H. Zhao, S. Zhang, G. Wu, G. J. Gordon, et al. Multiple source domain adaptation with adversarial learning. 2018.
- H. Zhao, R. T. Des Combes, K. Zhang, and G. Gordon. On learning invariant representations for domain adaptation. In *International Conference on Machine Learning*, pages 7523–7532. PMLR, 2019.
- S. Zhao, M. Gong, T. Liu, H. Fu, and D. Tao. Domain generalization via entropy regularization. *Advances in Neural Information Processing Systems*, 33, 2020.
- F. Zhou, Z. Jiang, C. Shui, B. Wang, and B. Chaib-draa. Domain generalization with optimal transport and metric learning. *arXiv preprint arXiv:2007.10573*, 2020.
- F. Zhou, Z. Jiang, C. Shui, B. Wang, and B. Chaib-draa. Domain generalization via optimal transport with metric similarity learning. *Neurocomputing*, 456:469–480, 2021a. ISSN 0925-2312. doi: <https://doi.org/10.1016/j.neucom.2020.09.091>. URL <https://www.sciencedirect.com/science/article/pii/S0925231221002009>.
- K. Zhou, Z. Liu, Y. Qiao, T. Xiang, and C. C. Loy. Domain generalization: A survey. *arXiv preprint arXiv:2103.02503*, 2021b.

A COMPARISON OF UPPER BOUNDS

A.1 Shortcomings of Previously Proposed Upper Bounds

First, recall that a *domain* v is a triple $(\mu^{(v)}, f^{(v)}, g^{(v)})$ consisting of a distribution $\mu^{(v)}$ on the inputs $\mathbf{x} \in \mathbb{R}^d$, a representation function that maps an input \mathbf{x} from input space to its representation \mathbf{z} in the representation space $f^{(v)} : \mathbb{R}^d \rightarrow \mathbb{R}^{d'}$, and a stochastic labeling function $g^{(v)} : \mathbb{R}^{d'} \rightarrow \mathcal{Y}$ maps the representation space $\mathbb{R}^{d'}$ to a label space \mathcal{Y} .

We denote the unseen domain by $(\mu^{(u)}, f^{(u)}, g^{(u)})$ and the seen domain by $(\mu^{(s)}, f^{(s)}, g^{(s)})$. Let $\mathcal{F} = \{f | f : \mathbb{R}^d \rightarrow \mathbb{R}^{d'}\}$ be a set of *representation functions*, $\mathcal{G} = \{g | g : \mathbb{R}^{d'} \rightarrow \mathcal{Y}\}$ a set of *stochastic labeling functions*. Here, the label space \mathcal{Y} is considered as binary. A *hypothesis* $h : \mathbb{R}^d \rightarrow \mathcal{Y}$ is obtained by composing each $g \in \mathcal{G}$ with each $f \in \mathcal{F}$, i.e., $h = g \circ f$. Next, we rewrite Theorem 1 in [Ben-David et al., 2007] using our notations.

Theorem 2. [Ben-David et al., 2007] *Let f be a fixed representation function from input space to representation space and \mathcal{G} be a hypothesis space of VC-dimension k . If a random labeled sample of size m is generated by applying f to i.i.d. samples from the seen domain, then with probability at least $1 - \delta$, for every $g \in \mathcal{G}$:*

$$R^{(u)}(g) \leq R^{(s)}(g) + d_{\mathcal{H}}(f_{\#}\mu^{(u)}, f_{\#}\mu^{(s)}) + \lambda \quad (11)$$

$$\leq \hat{R}^{(s)}(g) + \sqrt{\frac{4}{m} \left(k \log \frac{2em}{k} + \log \frac{4}{\delta} \right)} + d_{\mathcal{H}}(f_{\#}\mu^{(u)}, f_{\#}\mu^{(s)}) + \lambda \quad (12)$$

where e is the base of the natural logarithm, $d_{\mathcal{H}}$ is \mathcal{H} -divergence (please see Definition 1 in [Ben-David et al., 2010], Definition 2.1 in [Zhao et al., 2019] or Definition 1 in [Kifer et al., 2004]), $R^{(u)}(g) = \mathbb{E}_{\mathbf{z} \sim f_{\#}\mu^{(u)}} |g(\mathbf{z}) - g^{(u)}(\mathbf{z})|$ denotes the risk in the unseen domain, $R^{(s)}(g) = \mathbb{E}_{\mathbf{z} \sim f_{\#}\mu^{(s)}} |g(\mathbf{z}) - g^{(s)}(\mathbf{z})|$ and $\hat{R}^{(s)}(g)$ denote the risk in the seen domain and its empirical estimate, respectively, and:

$$\lambda = \inf_{g \in \mathcal{G}} (R^{(s)}(g) + R^{(u)}(g)) \quad (13)$$

is the combined risk.

Although the bound in Theorem 1 of [Ben-David et al., 2007] was originally constructed for the domain adaptation problem, it has significantly influenced past and recent work in domain generalization as discussed earlier in Section 1. To highlight the differences between our work and previous theoretical bounds (the bound in Theorem 1 of [Ben-David et al., 2007] and Theorem 4.1 of [Zhao et al., 2019]), we provide a detailed comparison below:

- First, Ben-David et al. [2007] define the risk induced by labeling function g from the representation space to the label space based on the disagreement between g and the optimal labeling function $g^{(u)}$:

$$R^{(u)}(g) = \mathbb{E}_{\mathbf{z} \sim f_{\#}\mu^{(u)}} |g(\mathbf{z}) - g^{(u)}(\mathbf{z})|. \quad (14)$$

On the other hand, we define the risk induced by using a hypothesis h from input space to label space by the disagreement between h and the optimal hypothesis $h^{(u)}$ via a general loss function

$\ell(\cdot, \cdot)$:

$$R^{(u)}(h) = \mathbb{E}_{\mathbf{x} \sim \mu^{(u)}} [\ell(h(\mathbf{x}), h^{(u)}(\mathbf{x}))]. \quad (15)$$

Since the empirical risk measures the probability of misclassification of a hypothesis that maps from the input space to the label space, minimizing $R^{(u)}(g)$ does not guarantee minimizing the empirical risk. Particularly, if the representation function f is invertible i.e., there is a one-to-one mapping between \mathbf{x} and \mathbf{z} , and the loss function $\ell(a, b) = |a - b|$, then it is possible to verify that $R^{(u)}(g) = R^{(u)}(h)$. In general, the representation map might not be invertible. For example, let us consider a representation function f that maps $f(\mathbf{x}_1) = f(\mathbf{x}_2) = \mathbf{z}$, $\mathbf{x}_1 \neq \mathbf{x}_2$, with corresponding labels given by $y_1 = 0$ and $y_2 = 1$. In this case, the risk defined in (14) will introduce a larger error than the risk introduced in (15) since $g(\mathbf{z})$ cannot be mapped to both "0" and "1". That said, the risk defined in (15) is more precise to describe the empirical risk. In addition, the risk defined in (14) is only a special case of (15) when the representation map f is invertible and the loss function satisfies $\ell(a, b) = |a - b|$.

- Second, for a given hypothesis space, the ideal joint hypothesis g^* is defined as the hypothesis which globally minimizes the combined error from seen and unseen domains [Ben-David et al., 2007, 2010]:

$$g^* = \arg \min_{g \in \mathcal{G}} (R^{(s)}(g) + R^{(u)}(g)).$$

In other words, this hypothesis should work well in both domains. Next, the error induced by using this ideal joint hypothesis is called *combined risk*:

$$\lambda = \inf_{g \in \mathcal{G}} (R^{(s)}(g) + R^{(u)}(g)) = (R^{(s)}(g^*) + R^{(u)}(g^*)).$$

Note that the labeling function is a mapping from the representation space to the label space, therefore the ideal labeling function g^* depends implicitly on the representation function f , hence, λ must depend on f . Simply ignoring this fact and treating λ as a constant may loosen the upper bound. In contrast, our goal is to construct an upper bound with the *combined risk* term $\sigma^{(u,s)}$ independent of both the representation function and the labeling function, which can be seen from Lemma 1 and Theorem 1.

Finally, it is worth comparing our upper bound with the bound in Theorem 4.1 of [Zhao et al., 2019] which also has the *combined risk* term free of the choice of the hypothesis class. However, note that the result in Theorem 4.1 of [Zhao et al., 2019] does not consider any representation function f , i.e., their labeling function directly maps from the input space to the label space, while our hypothesis is composed of a representation function from input space to representation space followed by a labeling function from representation space to label space. Since it is possible to pick a representation function f that maps any input to itself, i.e., $f(\mathbf{x}) = \mathbf{x}$ which leads to $h = g \circ f = g$, the bound in [Zhao et al., 2019] can be viewed as a special case of our proposed upper bound in Lemma 1.

A.2 Comparison with Upper Bounds in [Redko et al., 2017] and [Shen et al., 2018]

The form of the upper bound derived in Theorem 1 shares some similarities with Lemma 1 in [Redko et al., 2017] and Theorem 1 in [Shen et al., 2018], for example, all of them introduce Wasserstein distance between domain distributions. However, they differ in the following key aspects.

1. Our upper bound is constructed in the *representation* space, not in the data (ambient) space, which provides a theoretical justification for the risk of unseen domain when decomposing the hypothesis into a representation mapping and a labeling function. This is also consistent with the algorithmic implementation in practice.
2. The loss function in [Redko et al., 2017] is assumed to be convex, symmetric, bounded, obeying the triangle inequality, and satisfying a specific form, while in [Shen et al., 2018], it is required to be Lipschitz with respect to the hypothesis due to the use of Wasserstein-1 distance. With less constraints imposed on the loss function, we only assume it is symmetric, bounded, and satisfies the triangle inequality.
3. The bounds in Lemma 1 of [Redko et al., 2017] and Theorem 1 of [Shen et al., 2018] are controlled by the Wasserstein-1 distance while our upper bound is managed by the square-root of the Wasserstein-2 distance. There are regimes where one bound is tighter than the other. First, it is well-known that $W_1(\mu, \nu) \leq W_2(\mu, \nu)$, if $W_2(\mu, \nu) \leq 1$, then $W_1(\mu, \nu) \leq \sqrt{W_2(\mu, \nu)}$. However, based on Jensen's inequality, it is possible to show that $\sqrt{W_2(\mu, \nu)} \leq [Diam(f(\mathbf{X}))W_1(\mu, \nu)]^{1/4}$ where $Diam(f(\mathbf{X}))$ denotes the largest distance between two points in the representation space \mathbb{R}^d generated by input \mathbf{X} via mapping f . To guarantee $\sqrt{W_2(\mu, \nu)} \leq W_1(\mu, \nu)$, a sufficient condition is $[Diam(f(\mathbf{X}))W_1(\mu, \nu)]^{1/4} \leq W_1(\mu, \nu)$ which is equivalent to $Diam(f(\mathbf{X})) \leq W_1(\mu, \nu)^3$. In fact, for a given $Diam(f(\mathbf{X}))$, the larger the value of $W_1(\mu, \nu)$, the higher the chance that this sufficient condition will hold.

B PROOFS

B.1 Proof of Lemma 1

First, we want to note that our approach for constructing the upper bound in Lemma 1 is motivated by the proof of Theorem 1 in [Ben-David et al., 2010]. Next, to make the dependence on the hypothesis, input distribution, and the true representation and labeling functions transparent, we use inner product notation $\langle \cdot, \cdot \rangle$ to write expectations. Specifically,

$$R^{(v)}(h) := \mathbb{E}_{\mathbf{x} \sim \mu^{(v)}} [\ell(h(\mathbf{x}), h^{(v)}(\mathbf{x}))] = \langle \ell(h, h^{(v)}), \mu^{(v)} \rangle. \quad (16)$$

From the definition of risk,

$$\begin{aligned} R^{(u)}(h) &= \langle \ell(h, h^{(u)}), \mu^{(u)} \rangle = \langle \ell(h, h^{(s)}), \mu^{(s)} \rangle - \langle \ell(h, h^{(s)}), \mu^{(s)} \rangle + \langle \ell(h, h^{(u)}), \mu^{(u)} \rangle \\ &= R^{(s)}(h) + (\langle \ell(h, h^{(u)}), \mu^{(u)} \rangle - \langle \ell(h, h^{(s)}), \mu^{(u)} \rangle) + (\langle \ell(h, h^{(s)}), \mu^{(u)} \rangle - \langle \ell(h, h^{(s)}), \mu^{(s)} \rangle) \\ &\leq R^{(s)}(h) + \langle \ell(h^{(u)}, h^{(s)}), \mu^{(u)} \rangle + \langle \ell(h, h^{(s)}), \mu^{(u)} - \mu^{(s)} \rangle \end{aligned} \quad (17)$$

where (17) follows from the triangle inequality $\ell(h, h^{(u)}) \leq \ell(h, h^{(s)}) + \ell(h^{(s)}, h^{(u)})$ and because $\ell(h^{(s)}, h^{(u)}) = \ell(h^{(u)}, h^{(s)})$.

In an analogous fashion, it is possible to show that:

$$R^{(u)}(h) \leq R^{(s)}(h) + \langle \ell(h^{(u)}, h^{(s)}), \mu^{(s)} \rangle + \langle \ell(h, h^{(u)}), \mu^{(u)} - \mu^{(s)} \rangle. \quad (18)$$

Let $\mathbf{z} = f(\mathbf{x})$. Since f is invertible, $\mathbf{x} = f^{-1}(\mathbf{z})$. The third term in the right-hand side of (18) can be bounded as follows.

$$\begin{aligned} & \langle \ell(h, h^{(u)}), \mu^{(u)} - \mu^{(s)} \rangle \\ = & \langle \ell(g \circ f, g^{(u)} \circ f^{(u)}), \mu^{(u)} - \mu^{(s)} \rangle \\ = & \mathbb{E}_{\mathbf{x} \sim \mu^{(u)}} [\ell(g \circ f(\mathbf{x}), g^{(u)} \circ f^{(u)}(\mathbf{x}))] - \mathbb{E}_{\mathbf{x} \sim \mu^{(s)}} [\ell(g \circ f(\mathbf{x}), g^{(u)} \circ f^{(u)}(\mathbf{x}))] \\ = & \mathbb{E}_{\mathbf{z} \sim f_{\#}\mu^{(u)}} [\ell(g(\mathbf{z}), g^{(u)} \circ f^{(u)} \circ f^{-1}(\mathbf{z}))] - \mathbb{E}_{\mathbf{z} \sim f_{\#}\mu^{(s)}} [\ell(g(\mathbf{z}), g^{(u)} \circ f^{(u)} \circ f^{-1}(\mathbf{z}))] \\ = & \langle \ell(g, g^{(u)} \circ f^{(u)} \circ f^{-1}), f_{\#}\mu^{(u)} - f_{\#}\mu^{(s)} \rangle \\ \leq & L \langle 1, |f_{\#}\mu^{(u)} - f_{\#}\mu^{(s)}| \rangle \end{aligned} \quad (19)$$

where (19) follows from the assumption that the loss function is bounded by a positive number L and the fact that $f_{\#}\mu^{(u)} - f_{\#}\mu^{(s)} \leq |f_{\#}\mu^{(u)} - f_{\#}\mu^{(s)}|$.

Combining (18) and (19) we get,

$$R^{(u)}(h) \leq R^{(s)}(h) + \langle \ell(h^{(u)}, h^{(s)}), \mu^{(s)} \rangle + L \langle 1, |f_{\#}\mu^{(u)} - f_{\#}\mu^{(s)}| \rangle. \quad (20)$$

By similar reasoning, from (17),

$$R^{(u)}(h) \leq R^{(s)}(h) + \langle \ell(h^{(u)}, h^{(s)}), \mu^{(u)} \rangle + L \langle 1, |f_{\#}\mu^{(u)} - f_{\#}\mu^{(s)}| \rangle. \quad (21)$$

The proof of Lemma 1 now follows by combining (20) and (21) and noting that $\sigma^{(u,s)} = \min \left(\langle \ell(h^{(u)}, h^{(s)}), \mu^{(u)} \rangle, \langle \ell(h^{(u)}, h^{(s)}), \mu^{(s)} \rangle \right)$, and $\langle 1, |f_{\#}\mu^{(u)} - f_{\#}\mu^{(s)}| \rangle = \|f_{\#}\mu^{(u)} - f_{\#}\mu^{(s)}\|_1$.

B.2 Extension of Proof of Lemma 1 for Nearly Invertible Representation Maps

The proof of Lemma 1 requires that the representation map f is exactly invertible. However, this restricted condition can be relaxed. In practice, a function is called nearly invertible if there exists a reconstruction function with a sufficiently low reconstruction error. Based on the definition of nearly invertible maps, we can construct an upper bound similar to the one in Lemma 1 under some additional technical conditions that are discussed in what follows.

Let the representation map f be nearly invertible, i.e., there exists a function $s : \mathbb{R}^d \rightarrow \mathbb{R}^d$ such that if $f(\mathbf{x}) = \mathbf{z}$ then $\|\mathbf{x} - s(\mathbf{z})\| \leq \delta \forall \mathbf{z}$ where δ is a small positive constant. Suppose that $h^{(u)}$ is K -Lipschitz continuous. Then, $h^{(u)}(s(\mathbf{z})) - K\delta \leq h^{(u)}(\mathbf{x}) \leq h^{(u)}(s(\mathbf{z})) + K\delta$. Further suppose that the

cost function $\ell(\cdot, \cdot)$ is Q -Lipschitz continuous, i.e., $\ell(a, b) - Q|\gamma| \leq \ell(a, b + \gamma) \leq \ell(a, b) + Q|\gamma|$. Then,

$$\begin{aligned}
& \langle \ell(h, h^{(u)}), \mu^{(u)} - \mu^{(s)} \rangle \\
&= \langle \ell(g \circ f, g^{(u)} \circ f^{(u)}), \mu^{(u)} - \mu^{(s)} \rangle \\
&= \mathbb{E}_{\mathbf{x} \sim \mu^{(u)}} \left[\ell(g \circ f(\mathbf{x}), h^{(u)}(\mathbf{x})) \right] - \mathbb{E}_{\mathbf{x} \sim \mu^{(s)}} \left[\ell(g \circ f(\mathbf{x}), h^{(u)}(\mathbf{x})) \right] \\
&\leq \max \left\{ \mathbb{E}_{\mathbf{z} \sim f_{\#}\mu^{(u)}} \left[\ell(g(\mathbf{z}), h^{(u)}(s(\mathbf{z})) + K\delta) \right], \mathbb{E}_{\mathbf{z} \sim f_{\#}\mu^{(u)}} \left[\ell(g(\mathbf{z}), h^{(u)}(s(\mathbf{z})) - K\delta) \right] \right\} \\
&\quad - \min \left\{ \mathbb{E}_{\mathbf{z} \sim f_{\#}\mu^{(s)}} \left[\ell(g(\mathbf{z}), h^{(u)}(s(\mathbf{z})) + K\delta) \right], \mathbb{E}_{\mathbf{z} \sim f_{\#}\mu^{(s)}} \left[\ell(g(\mathbf{z}), h^{(u)}(s(\mathbf{z})) - K\delta) \right] \right\} \\
&\leq \mathbb{E}_{\mathbf{z} \sim f_{\#}\mu^{(u)}} \left[\ell(g(\mathbf{z}), g^{(u)} \circ f^{(u)}(s(\mathbf{z}))) \right] - \mathbb{E}_{\mathbf{z} \sim f_{\#}\mu^{(s)}} \left[\ell(g(\mathbf{z}), g^{(u)} \circ f^{(u)}(s(\mathbf{z}))) \right] \\
&\quad + \mathbb{E}_{\mathbf{z} \sim f_{\#}\mu^{(u)}} \left[QK\delta \right] + \mathbb{E}_{\mathbf{z} \sim f_{\#}\mu^{(s)}} \left[QK\delta \right] \\
&\leq \langle \ell(g, g^{(u)}), f_{\#}\mu^{(u)} - f_{\#}\mu^{(s)} \rangle + QK\delta + QK\delta \\
&\leq L \langle 1, |f_{\#}\mu^{(u)} - f_{\#}\mu^{(s)}| \rangle + 2QK\delta
\end{aligned} \tag{22}$$

where the fourth inequality due to the assumption that $\ell(\cdot, \cdot)$ is a distance metric, both $g(\cdot)$ and $g^{(u)}(\cdot)$ map \mathbf{z} to 1-dimension space and the fact that $h^{(u)}(s(\mathbf{z})) - K\delta \leq h^{(u)}(\mathbf{x}) \leq h^{(u)}(s(\mathbf{z})) + K\delta$, the fifth inequality due to $\ell(\cdot, \cdot)$ is Q -Lipschitz, and the last inequality due to $\ell(\cdot, \cdot)$ is bounded by L . In comparison to the original result in Lemma 1, one more term ($2QK\delta$) is introduced in the upper bound if the representation map is nearly invertible. If $\delta = 0$, $\forall \mathbf{z}$, or in other words, the representation map is exactly invertible, then the extra term $2QK\delta$ is, of course, zero.

B.3 Proof of Lemma 3

From Pinsker's inequality [Berend et al., 2014, Csiszár and Körner, 2011], the L^1 distance can be bounded by Kullback–Leibler (KL) divergence as follows:

$$\|\mu - \nu\|_1^2 \leq 2d_{KL}(\mu, \nu) \tag{23}$$

where $\|\mu - \nu\|_1$ and $d_{KL}(\mu, \nu)$ denote L^1 distance and Kullback–Leibler divergence between two distributions μ and ν , respectively. Since $\|\mu - \nu\|_1 = \|\nu - \mu\|_1$, using Pinsker's inequality for (μ, ν) and (ν, μ) ,

$$2\|\mu - \nu\|_1^2 = \|\mu - \nu\|_1^2 + \|\nu - \mu\|_1^2 \leq 2d_{KL}(\mu, \nu) + 2d_{KL}(\nu, \mu) \tag{24}$$

which is equivalent to,

$$\|\mu - \nu\|_1 \leq \sqrt{d_{KL}(\mu, \nu) + d_{KL}(\nu, \mu)}. \tag{25}$$

Next, if μ and ν are (c_1, c_2) -regular distributions, their Kullback–Leibler divergences can be bounded by their Wasserstein-2 distance as follows (please see equation (10), Proposition 1 in [Polyanskiy and Wu, 2016]),

$$d_{KL}(\mu, \nu) + d_{KL}(\nu, \mu) \leq 2 \left(\frac{c_1}{2} \sqrt{\mathbb{E}_{\mathbf{u} \sim \mu} [\|\mathbf{u}\|_2^2]} + \frac{c_1}{2} \sqrt{\mathbb{E}_{\mathbf{v} \sim \nu} [\|\mathbf{v}\|_2^2]} + c_2 \right) [\mathbb{W}_2(\mu, \nu)]. \tag{26}$$

Combining (25) and (26),

$$\|\mu - \nu\|_1 \leq \sqrt{c_1 \left(\sqrt{\mathbb{E}_{\mathbf{u} \sim \mu} [\|\mathbf{u}\|_2^2]} + \sqrt{\mathbb{E}_{\mathbf{v} \sim \nu} [\|\mathbf{v}\|_2^2]} \right) + 2c_2} [\mathbb{W}_2(\mu, \nu)]^{1/2}. \tag{27}$$

B.4 Proof of Theorem 1

Under the assumption that $f_{\#\mu^{(s)}}$ and $f_{\#\mu^{(u)}}$ are (c_1, c_2) -regular $\forall s = 1, 2, \dots, S$, from Lemma 3,

$$\begin{aligned} \|f_{\#\mu^{(u)}} - f_{\#\mu^{(s)}}\|_1 &\leq \sqrt{c_1 \left(\sqrt{\mathbb{E}_{\mathbf{x} \sim \mu^{(s)}} [\|f(\mathbf{x})\|_2^2]} + \sqrt{\mathbb{E}_{\mathbf{x} \sim \mu^{(u)}} [\|f(\mathbf{x})\|_2^2]} \right) + 2c_2} \\ &\quad \times [\mathbf{W}_2(f_{\#\mu^{(u)}}, f_{\#\mu^{(s)}})]^{1/2}. \end{aligned} \quad (28)$$

Let:

$$C := \max_{s \in \{1, \dots, S\}} \sqrt{c_1 \left(\sqrt{\mathbb{E}_{\mathbf{x} \sim \mu^{(s)}} [\|f(\mathbf{x})\|_2^2]} + \sqrt{\mathbb{E}_{\mathbf{x} \sim \mu^{(u)}} [\|f(\mathbf{x})\|_2^2]} \right) + 2c_2}. \quad (29)$$

Multiplying (28) by $\lambda^{(s)}$ and summing over all s we get:

$$\sum_{s=1}^S \lambda^{(s)} \|f_{\#\mu^{(u)}} - f_{\#\mu^{(s)}}\|_1 \leq C \sum_{s=1}^S \lambda^{(s)} [\mathbf{W}_2(f_{\#\mu^{(u)}}, f_{\#\mu^{(s)}})]^{1/2}. \quad (30)$$

By Jensen's inequality,

$$\sum_{s=1}^S \lambda^{(s)} [\mathbf{W}_2(f_{\#\mu^{(u)}}, f_{\#\mu^{(s)}})]^{1/2} \leq \left[\sum_{s=1}^S \lambda^{(s)} \mathbf{W}_2^2(f_{\#\mu^{(u)}}, f_{\#\mu^{(s)}}) \right]^{1/4}. \quad (31)$$

From (30) and (31),

$$\sum_{s=1}^S \lambda^{(s)} \|f_{\#\mu^{(u)}} - f_{\#\mu^{(s)}}\|_1 \leq C \left[\sum_{s=1}^S \lambda^{(s)} \mathbf{W}_2^2(f_{\#\mu^{(u)}}, f_{\#\mu^{(s)}}) \right]^{1/4}. \quad (32)$$

Finally, combining the upper bound in Lemma 2 and (32), the proof follows.

C DATASETS, IMPLEMENTATION DETAILS AND ADDITIONAL EXPERIMENTS

C.1 Datasets

- **Office-Caltech:** Office-Caltech [Gong et al., 2012] dataset consists of 2533 images from 4 different domains: Amazon (A), Webcam (W), Caltech-256 (C), and DSLR (D), where a total of 10 classes are shared by all domains. We use the 4096-dimensional DeCAF₆ features [Donahue et al., 2014] as input.
- **Office-Home:** Office-Home dataset [Venkateswara et al., 2017] is a larger dataset with 15,500 images from 4 different domains: Artistic images (A), Clip Art (C), Product images (P), and Real-World (R). Each domain has 65 common object categories. Here we extract ResNet-50 deep features of each domain by an ImageNet pre-trained ResNet-50 model with the last fully connected (FC) layer is replaced by a linear layer with the output dimension of 65. With one of the four domains treated as the unseen domain, the data from the aggregation of the remaining three seen domains is split into training and validation sets (80%/20%). The ResNet-50 model

is then fine-tuned using the training data with cross-entropy loss for 50 epochs. We select the model with the lowest validation loss as the final deep feature extractor for the selected unseen domain. The above procedure is repeated four times till deep features of all four domains are obtained.

- **Rotated MNIST:** The rotated MNIST contains 6 different domains, with each domain containing 1000 digit images rotated by $0^\circ, 15^\circ, 30^\circ, 45^\circ, 60^\circ, 75^\circ$ of the original MNIST images. The dataset is constructed as follows: 100 samples are randomly chosen from each of 10 classes from the original MNIST as domain M_0 . We then adopt the way described by Gulrajani and Lopez-Paz [2020] to construct domains $M_{15}, M_{30}, M_{45}, M_{60}, M_{75}$, which deviate from the conventional Rotated MNIST dataset [Ghifary et al., 2015, Zhao et al., 2020, Ilse et al., 2020]. Specifically, instead of rotating the same group of images belonging to M_0 as conducted in [Ghifary et al., 2015, Zhao et al., 2020, Ilse et al., 2020], we remove images that have already been chosen for M_0 from MNIST dataset, sample another 1000 images (100 for each class), and rotate by 15° to form M_{15} . The above procedure is repeated for the remaining domains.

C.2 Implementation Details for Comparison Methods

- **ERM:** The Empirical Risk Minimization method serves as a baseline method. We train a feature extractor and a classifier on the data from all seen domains without performing any DG techniques. The feature extractor and classifier are trained together using cross-entropy loss with a batch size of 64 for all the datasets.
- **MLDG** [Li et al., 2018a]: The meta-learning DG approach divides multiple seen domains into meta-train and meta-test domains to mimic domain shift and conducts optimization to improve model performance over meta-train and meta-test data. We reference the implementation in DomainBed [Gulrajani and Lopez-Paz, 2020] for meta-learning optimization. Each batch is formed by 50 samples equally picked from each seen domain for Office-Caltech and Rotated MNIST datasets and doubled for Office-Home dataset.
- **DANN** [Ganin et al., 2016]: The domain adversarial neural network is a DA method which trains a domain-invariant feature extractor together with a domain discriminator via adversarial training process. It is widely used in DA problems and the idea of learning a domain-invariant representation motivated some of the adversarial approaches in DG. We reference a recent GitHub project ¹ for the gradient reversal layer implementation and DomainBed [Gulrajani and Lopez-Paz, 2020] for the training process. The batch size is adjusted such that same number of batches are formed for both seen and unseen domain.
- **MMD-AAE** [Li et al., 2018b]: The maximum mean discrepancy (MMD)-adversarial autoencoder aligns the representation distributions from different domains via minimizing their MMD and matches the learned representation distribution to a prior distribution in an adversarial manner.

¹https://github.com/fungtion/DANN_py3

Since the code is not released from the author, we reference DomainBed [Gulrajani and Lopez-Paz, 2020] for the MMD loss calculation and implement the other part of the algorithm by ourselves. Following the original MMD-AAE paper, we choose the prior distribution as Laplace distribution for adversarial training. For MMD estimation, a mixture kernel is used via averaging the RBF kernels with the bandwidth $\sigma = 1, 5, 10$, as also suggested in the original paper [Li et al., 2018b]. The batch size is set to be the same as that for MLDG.

C.3 Models for Each Dataset

The feature extractor for Office-Caltech and Office-Home has three fully connected (FC) layers (Input $\rightarrow 1024 \rightarrow 512 \rightarrow 100$ for Office-Caltech, and input $\rightarrow 1024 \rightarrow 512 \rightarrow 200$ for Office-Home) with ReLU as the activation function. For Rotated MNIST, we adopt a typical MNIST-CNN model structure with three 2-D convolutional layers. The kernel, stride, and padding sizes for each layer are set to be 3, 2, 1, with the number of output channels set as 16, 16, 10. The decoder shares the same structure as the encoder but in reverse order (for convolutions layer, it becomes ConvTranspose2d). The classifier is a one-linear-layer model with the output dimension the same as the number of classes. Another one-linear-layer model serves as the domain discriminator for the adversarial-based methods with the output size as 2. The above model structures are the same for both comparison and proposed methods.

Table 5: Performance on Rotated MNIST Dataset

| Unseen | M_0 | M_{15} | M_{30} | M_{45} | M_{60} | M_{75} | Avg |
|---------|-----------------------|-----------------------|-----------------------|-----------------------|-----------------------|-----------------------|-----------------------|
| ERM | 74.7 \pm 0.5 | 93.0 \pm 0.9 | 93.8 \pm 0.7 | 93.8 \pm 0.6 | 92.6 \pm 1.0 | 78.4 \pm 1.9 | 87.7 \pm 1.0 |
| DANN | 74.2 \pm 1.0 | 92.6 \pm 0.4 | 92.6 \pm 0.2 | 93.0 \pm 0.4 | 91.3 \pm 0.4 | 78.5 \pm 0.4 | 87.1 \pm 0.5 |
| MMD-AAE | 73.9 \pm 2.0 | 92.0 \pm 0.9 | 92.9 \pm 0.8 | 93.4 \pm 0.7 | 92.2 \pm 1.4 | 77.8 \pm 0.9 | 87.0 \pm 1.2 |
| MLDG | 75.7 \pm 0.8 | 93.1 \pm 0.2 | 93.5 \pm 0.6 | 93.9 \pm 0.3 | 92.7 \pm 0.3 | 80.2 \pm 1.3 | 88.2 \pm 0.7 |
| WBAE | 76.1 \pm 1.6 | 94.4 \pm 0.7 | 94.9 \pm 0.5 | 94.8 \pm 0.8 | 93.9 \pm 0.7 | 81.0 \pm 0.5 | 89.2 \pm 0.9 |
| WBMI | 77.8 \pm 0.8 | 94.1 \pm 0.4 | 94.9 \pm 0.8 | 94.6 \pm 0.4 | 92.9 \pm 0.3 | 80.4 \pm 0.9 | 89.1 \pm 0.6 |

Table 6: Ablation Study for Rotated MNIST Dataset

| Unseen | ERM | WBAE- L_{wb} | WBAE- L_r WBMI- L_i | WBAE | WBMI |
|----------|----------------|----------------|----------------------------|----------------------------------|----------------------------------|
| M_0 | 74.7 ± 0.5 | 74.2 ± 0.7 | 76.5 ± 1.2 | 76.1 ± 1.6 | 77.8 ± 0.8 |
| M_{15} | 93.0 ± 0.9 | 93.0 ± 0.2 | 94.2 ± 0.6 | 94.4 ± 0.7 | 94.1 ± 0.4 |
| M_{30} | 93.8 ± 0.7 | 93.9 ± 0.6 | 94.6 ± 0.6 | 94.9 ± 0.5 | 94.9 ± 0.8 |
| M_{45} | 93.8 ± 0.6 | 94.0 ± 0.6 | 94.5 ± 0.5 | 94.8 ± 0.8 | 94.6 ± 0.4 |
| M_{60} | 92.6 ± 1.0 | 92.6 ± 0.4 | 93.7 ± 0.4 | 93.9 ± 0.7 | 92.9 ± 0.3 |
| M_{75} | 78.4 ± 1.9 | 79.3 ± 0.5 | 80.0 ± 0.5 | 81.0 ± 0.5 | 80.4 ± 0.9 |
| Average | 87.7 ± 1.0 | 87.8 ± 0.5 | 88.9 ± 0.7 | 89.2 ± 0.9 | 89.1 ± 0.6 |

C.4 Results and Ablation Study for Rotated MNIST

Training Procedure: All models are trained for 400 epochs using the Adam optimizer [Kingma and Ba, 2015] with the learning rate set as 5×10^{-4} . The hyper-parameter tuning, model selection strategy and evaluation process are the same as we did for Office-Caltech and Office-Home datasets. The (α, β) pair is chosen to be (0.01, 0.01) for both WBAE and WBMI methods.

The performance of the proposed methods on Rotated MNIST dataset is shown in Table 5 and the ablation study can be found in Table 6.